Inorganic Chemistry

Article

Cite This: Inorg. Chem. 2018, 57, 7665−7675

pubs.acs.org/IC

Enhanced Photostability Luminescent Properties of Er^{3+}-Doped Near-White-Emitting $Dy_xEr_{(1-x)}$-POM Derivatives

Hechen Wu, Bing Yan, Huafeng Li, Vikram Singh, Pengtao Ma,* Jingyang Niu, and Jingping Wang*

Henan Key Laboratory of Polyoxometalate Chemistry, College of Chemistry and Chemical Engineering, Henan University, Kaifeng, Henan 475004, China

Supporting Information

ABSTRACT: A series of $Dy_xEr_{(1-x)}$-polyoxometalates (POMs) were successfully synthesized and characterized well by various physicochemical analysis. The structurally isolated compounds exhibit three characteristic emissions at 480 nm (blue, $^4F_{9/2} \rightarrow {}^6H_{15/2}$ transition), 573 nm (yellow, $^4F_{9/2} \rightarrow {}^6H_{13/2}$ transition), and 663 nm (red, $^4F_{9/2} \rightarrow {}^6H_{11/2}$ transition) whose luminescent color coordinates appear in the near-white area in the CIE 1931 chromaticity diagram. Time-resolved emission spectroscopy was used in $Dy_xEr_{(1-x)}$-POM to further authenticate energy transfer from the photoexcitation O → M ligand to the metal charge-transfer state of phosphotungstate components to active Dy^{3+}/Er^{3+} ions and energy transfer between Dy^{3+} ion and Er^{3+} ion via intramolecular energy transitions. The relative emission intensity of ∼32%, ∼53%, and ∼85% for Dy-POM, $Dy_{0.9}Er_{0.1}$-POM, and $Dy_{0.8}Er_{0.2}$-POM respectively, were obtained under 300 min of UV irradiation, which indicates better photostability of $Dy_{0.8}Er_{0.2}$-POM. Furthermore, $Dy_xEr_{(1-x)}$-POM samples can emit macroscopic white light under blue irradiation.

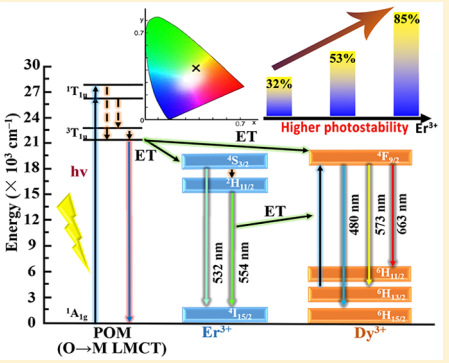

INTRODUCTION

Polyoxometalates (POMs) are a class of discrete metal−oxygen clusters of high oxidation states transition metals (e.g., V^{5+}, Nb^{5+}, Ta^{5+}, Mo^{6+}, W^{6+}). Insertion of additional heteroatoms (e.g., B, Si, P, Ge, As, Se, Sb, or Te) in the polyanionic framework may induce noticeable characteristic changes in their properties such as (a) improved solid state thermal stability; (b) modified structural topologies; (c) inducing more nucleophilic oxygen enriched surfaces for interesting electronic properties achieved by compositional variations on POM skeletons; (d) ease of binding for d- and f-metal ions via inorganic multidentate O-donor ligands either through O- and N-donor functional organic moieties.[1−4] POMs are well-defined with abundant structural topologies and are thus employed in diverse areas of research such as magnetic materials, photoluminescence, catalysis, medicinal chemistry, and materials science.[5,6]

It is well-known that lanthanide ion (Ln^{3+})-based complexes are excellent inorganic optical materials and have drawn considerable interest of researchers because of their sharp characteristic emissions, long luminescent lifetime, potentially high quantum efficiency, good reliability, and safety. On account of these excellent features, Ln^{3+}-based materials have been employed in various optical applications such as lighting diodes, detection and sensing, lasers, bioimaging, biomedical analysis, etc.[7−10] Until now, Ce^{3+}-, Dy^{3+}-, Er^{3+}-, Sm^{3+}-, Tm^{3+}-, Yb^{3+}-, Pr^{3+}-, and Eu^{3+}-based materials have been scientifically explored and partially commercialized in lighting and display purposes in various disciplines of technology.[11−13] Interestingly, the luminescence of Ln^{3+} is restricted due to the electric-dipole-forbidden nature of f−f transitions within the unfilled 4f shells, which may lead to small molar absorption coefficients (ε < 10 L $mol^{-1}cm^{-1}$) and long luminescence lifetime.[14,15] Although some magnetic-dipole f−f transitions of Ln^{3+} are allowed, their intensity is too weak to implement their use in practical applications.[16] The alternative route to overcome such discrepancies like small absorption coefficients is to sensitize Ln^{3+} emissions through appropriate sensitizers, which can eventually involve light harvesting and subsequent energy transfer to the Ln^{3+} via antenna effect.[17,18] Fortunately, Ln^{3+} ions can be utilized as a good electron acceptors due to unfilled 5d or 6s orbitals which can accept lone pair of electrons from various ligands to form covalent bonds.[19,20] Moreover, the luminescence of Ln^{3+}-based materials are influenced by the following: (1) high concentration of Ln^{3+} in complexes which may lead to quenching in luminescence intensity; (2) the ligands such as aqua or similar solvent when coordinated to Ln^{3+} would quench the luminescence due to the high frequency of O−H or N−H stretching vibrations; (3) some emitting Ln^{3+} ions are sensitive to field effects such as highly symmetrical coordination and molecular symmetry around Ln^{3+} centers.[21−23]

Since the advent of the first Ln^{3+}-based POMs (Ln-POMs) by Peacock and Weakley in 1971, more and more attention has been attracted to the synthesis of Ln-POMs complexes because of their potential catalysis, magnetism, and optical properties.[24−27] Over the years, a large range of mono-, di-, tri-, tetra-,

Received: March 13, 2018
Published: June 18, 2018

DOI: 10.1021/acs.inorgchem.8b00674
Inorg. Chem. 2018, 57, 7665−7675

and even up to 24 nuclearity Ln-POMs structures with outstanding properties have been consistently reported.[28] With regard to optical properties, POMs are appropriate light-harvesting candidates as upon irradiation they can act as antenna ligands to sensitize inherently small absorption Ln^{3+} centers through intramolecular energy transfer from the O → M photoexcitation state of ligand to metal charge transfer (LMCT) state within Ln-POMs molecules. The luminescent Ln-POMs can potentially be applied in photochromic, sensors, lighting materials, and so on. For example, Boskovic and co-workers reported that several luminescent Ln-POMs complexes, which can be potentially regarded as inorganic Ln-based phosphors, have been used to explore the energy transfer mechanism in Ln-POM complexes.[29,30] Zhao and co-workers synthesized a series of Ln-POMs and deeply investigated their photoluminescence (PL) properties.[31−34] Our group also actively engaged in this direction and obtained a great deal of Ln-POMs derivatives that display obvious photochromic or PL properties under xenon lamp irradiation.[35−43]

Although a large number of Ln-POMs complexes have been reported, still there are relatively far less studies on mixed Ln/Ln′-POMs complexes. In recent years, a few reports on mixed Ln/Ln′ ions in an appropriate ratio within the same Ln-POMs complexes have been documented. In 2013, Sato et al. successfully synthesized heterodinuclear Ln/Ln′-POMs $TBA_8H_4[\{Ln(\mu_2\text{-}OH)_2Ln'\}(\gamma\text{-}SiW_{10}O_{36})_2]$ (Ln = Dy and Gd; Ln′ = Eu, Yb, and Lu). The study of $TBA_8H_4[\{Dy(\mu_2\text{-}OH)_2Ln'\}(\gamma\text{-}SiW_{10}O_{36})_2]$ showed single-molecule magnet (SMM) behavior due to the strong magnetic anisotropy of the Dy^{3+} ion, and the energy barriers for magnetization reversal can be operated via a change in coordination geometry of the Dy^{3+} ion by tuning the types and ratio of the Ln′ ion.[44] Shiddip et al. obtained other Ln/Ln′-POMs $Na_9[Ho_xY_{(1-x)}(W_5O_{18})_2]\cdot H_2O$ (x = 0.001−0.25) that exhibits clock transitions which can be treated as a method of enhancing coherence of molecular spin qubits in 2016.[45] These studies of Ln/Ln′-POMs materials were mainly based on magnetic properties. In addition, several luminescent Ln/Ln′-POMs materials were also investigated. In 2012, Wu and co-workers successfully obtained dinuclear Ln-POMs $\{[Ln_2(DMF)_8(H_2O)_6][ZnW_{12}O_{40}]\}\cdot 4DMF$ (Ln = La, Eu and Tb) and heterodinuclear Ln/Ln′-POMs $\{[Ln_{(1-x)}Ln'_x(DMF)_8(H_2O)_6][ZnW_{12}O_{40}]\}\cdot 4DMF$ (Ln = Tb; Ln′ = Eu; x = 0, 0.25, 0.5, 0.75 and 1.0). The results prove that the CIE luminescent color coordinates could be manipulated by adjusting the ratios of Eu^{3+} and Tb^{3+} ions. The calculated CIE 1931 chromaticity coordinates for $Tb_{0.25}Eu_{0.75}$-POMs (0.342, 0.362) are near standard white light (0.33, 0.33).[46] In 2017, Kaczmarek et al. discussed the luminescence properties of hetero-tetranuclear Ln/Ln′-POMs $[Ln_{(4-x)}Ln'_x(MoO_4)(Mo_7O_{24})_4]^{14-}$ (Ln = La; Ln′ = Eu^{3+}, Tb^{3+}, Sm^{3+}, Dy^{3+}, and Nd^{3+}; x = 0.05) and tetranuclear Ln-POMs $[Ln_4(MoO_4)(Mo_7O_{24})_4]^{14-}$ (Ln = Eu^{3+}, Tb^{3+}, Sm^{3+}, Dy^{3+}, and Nd^{3+}). The results indicate that La-POMs doped with emissive Ln^{3+} ions could display good luminescence properties that can be potentially employed as visible and NIR luminescent materials.[47] In the same year, Kaczmarek et al. obtained other hetero-multinuclear Ln/Ln′-POMs $[Tb_{3.94}Eu_{0.06}(MoO_4)(Mo_7O_{24})_4]^{14-}$ and $[Tb_{3.68}Eu_{0.32}(MoO_4)(Mo_7O_{24})_4]^{14-}$, which can display outstanding temperature-dependent luminescence properties. Especially, $[Tb_{3.94}Eu_{0.06}(MoO_4)(Mo_7O_{24})_4]^{14-}$ shows excellent temperature-dependent luminescence property particularly in the low temperature region which is highly significant for industrial applications in the energy and aerospace industries.[48] Besides, Zhou and co-workers reported a series of heteronuclear Eu/Tb/La-POMs $Na(HL)(CH_3COO)Eu_mTb_nLa_{1-m-n}(AlMo_6(OH)_6O_{18})(H_2O)_6\cdot 10H_2O$ (L = nicotinate) that exhibit tunable luminescence color, and the white light emitting can be realized through an appropriate molar ratio of Eu/Tb/La.[49] Thus, the background offers us a good opportunity to further explore heteronuclear Ln/Ln′-POMs materials.

In this work, we choose the reported $[N(CH_3)_4]_6K_3H_7[Dy(C_4H_2O_6)(\alpha\text{-}PW_{11}O_{39})]_2\cdot 27H_2O$ as the parent Ln-POM (Dy-POM),[42] and a series of different ratios of Er^{3+} ion doped $Dy_xEr_{(1-x)}$-POM (x = 0−1) derivatives which have been well synthesized. The structure of $Dy_xEr_{(1-x)}$-POM were characterized by elemental analysis, powder X-ray diffraction (PXRD), thermogravimetric analyses (TGA), energy dispersive X-ray spectroscopy (EDX), inductively coupled plasma atomic emission spectrometer (ICP-AES), and IR spectra. The schematic energy level diagram is proposed to demonstrate the process of energy transfer and characteristic emissions of Dy^{3+} and Er^{3+} ions in $Dy_xEr_{(1-x)}$-POM. Furthermore, the time-resolved emission spectroscopy was measured to authenticate the mechanism involved in the energy transfer process. Photostability of PL of $Dy_xEr_{(1-x)}$-POM has been systematically investigated, and the PL lifetime, emitting colors in the CIE 1931 chromaticity diagram, color purity, and correlated color temperature (CCT) have also been investigated in this work. The study reveals that Er^{3+}-doped $Dy_xEr_{(1-x)}$-POM samples possess relatively good photostability as compared to pure Dy-POM.

EXPERIMENTAL SECTION

Materials and Methods. All chemicals were commercially purchased and used without further purification. The precursor $K_{14}[P_2W_{19}O_{69}(H_2O)]\cdot 24H_2O$ was synthesized according to the literature and confirmed by IR spectroscopy.[42] C, H, and N elemental analyses were recorded using an Elementar Vario EL cube CHNS analyzer. Analyses for P, W, Dy, and Er atoms were conducted on a PerkinElmer Optima 2000 ICP-OES spectrometer (Table S1). PXRD data were recorded on an X-ray powder diffractometer (Bruker, D8 Advance) using Cu Kα radiation (λ = 1.5418 Å) collected with the angular range (2θ) from 5° to 45° at room temperature. IR spectra were measured on a Bruker VERTEX-70 spectrometer using KBr pellets in the range of 400−4000 cm^{-1}. EDX measurements were recorded on a JSM-7610F scanning electron microscope with an OXFORD x-act EDS system (Figures S1 and S2). TGA was performed in flowing N_2 from room temperature to 800 °C at a heating rate of 10 °C min^{-1} on a NETZSCH STA 449 F5 Jupiter thermal analyzer (Figure S3). Crystallographic parameters were measured on a Bruker Apex II CCD diffractometer at room temperature with the graphite-monochromated Mo Kα radiation (λ = 0.71073 Å). PL emission spectra, PL excitation spectra, and decay time curves were performed on an EDINBURGH FLS 980 fluorescence spectrophotometer equipped with a monochromated 325 W Xe-arc excitation source and a visible detector (Hamamatsu R928P). PL photographs were taken with an entrance slit of 1 mm and an exit slit of 1 mm. The CIE 1931 chromaticity coordinates, dominant wavelength, color purity, and CCT were calculated on account of the international CIE standards. The distance between the sample and xenon lamp is 50 cm during the measurement of photostability.

Synthesize of $[N(CH_3)_4]_6K_3H_7[Dy(C_4H_2O_6)(\alpha\text{-}PW_{11}O_{39})]_2\cdot 27H_2O$ (Dy-POM). $DyCl_3\cdot 6H_2O$ (0.228 g, 0.600 mmol) was dissolved in deionized water (30 mL), and then tartaric acid (0.120 g, 0.800 mmol) was added. The resulting solution stirred to form a clear solution, followed by the solid addition of $K_{14}[P_2W_{19}O_{69}(H_2O)]\cdot 24H_2O$ (2.120 g, 0.465 mmol) at room temperature. Finally, the pH value of solution was adjusted to 3.2 by 3 mol L^{-1} KOH solution. This

DOI: 10.1021/acs.inorgchem.8b00674
Inorg. Chem. 2018, 57, 7665−7675

solution was stirred and heated to 60 °C for 1.5 h, and subsequently tetramethylammonium chloride (TMACl) (0.110 g, 1.000 mmol) was added and stirred for another 30 min. The resulting solution was cooled and filtered to evaporate at room temperature. The clear filtrate was left for about 2 weeks to obtain colorless block crystals. Yield: 33.6% (0.707 g, based on $DyCl_3·6H_2O$). Selected IR (KBr, cm^{-1}): 3445 (br), 3041 (w), 1622 (s), 1486 (s), 1094 (s), 1049 (s), 952 (s), 889 (s), 829 (s) and 715 (w). Elemental analyses (%): Calcd, C, 5.47; H, 1.97; N, 1.20; Found, C, 5.49; H, 1.69; N, 1.23.

Synthesis of $[N(CH_3)_4]_6K_3H_7[Dy_xEr_{1-x}(C_4H_2O_6)(\alpha\text{-}PW_{11}O_{39})]_2·27H_2O$ (Dy_xEr_{1-x}-POM). The synthesis of Dy_xEr_{1-x}-POM is similar to Dy-POM except for $DyCl_3·6H_2O$ replaced by the mixture of $DyCl_3·6H_2O$ and $ErCl_3·6H_2O$ in rational proportions (see the Supporting Information). Er-POM: selected IR (KBr, cm^{-1}): 3453 (br), 3030 (w), 1624 (s), 1484 (s), 1100 (s), 1050 (s), 952 (s), 888 (s), 820 (s) and 720 (w); elemental analyses (%): Calcd, C, 5.46; H, 1.96; N, 1.19; Found, C, 5.79; H, 1.86; N, 1.29. $Dy_{0.9}Er_{0.1}$-POM: selected IR (KBr, cm^{-1}): 3450 (br), 3038 (w), 1619 (s), 1485 (s), 1101 (s), 1050 (s), 952 (s), 890 (s), 829 (s) and 727 (w); elemental analyses (%): Calcd, C, 5.47; H, 1.96; N, 1.20; Found, C, 5.39; H, 1.64; N, 1.11. $Dy_{0.8}Er_{0.2}$-POM: selected IR (KBr, cm^{-1}): 3444 (br), 3041 (w), 1619 (s), 1485 (s), 1104 (s), 1051 (s), 952 (s), 890 (s), 823 (s) and 724 (w); elemental analyses (%): Calcd, C, 5.47; H, 1.96; N, 1.20; Found, C, 5.61; H, 1.70; N, 1.26. $Dy_{0.7}Er_{0.3}$-POM: selected IR (KBr, cm^{-1}): 3450 (br), 3036 (w), 1621 (s), 1486 (s), 1095 (s), 1048 (s), 952 (s), 888 (s), 824 (s) and 720 (w); elemental analyses (%): Calcd, C, 5.47; H, 1.96; N, 1.20; Found, C, 5.52; H, 1.85; N, 1.32. $Dy_{0.6}Er_{0.4}$-POM: selected IR (KBr, cm^{-1}): 3446 (br), 3038 (w), 1624 (s), 1487 (s), 1095 (s), 1049 (s), 952 (s), 888 (s), 824 (s) and 717 (w); elemental analyses (%): Calcd, C, 5.47; H, 1.96; N, 1.20; Found, C, 5.48; H, 1.78; N, 1.28. $Dy_{0.5}Er_{0.5}$-POM: selected IR (KBr, cm^{-1}): 3455 (br), 3040 (w), 1618 (s), 1486 (s), 1093 (s), 1049 (s), 952 (s), 889 (s), 820 (s) and 716 (w); elemental analyses (%): Calcd, C, 5.47; H, 1.96; N, 1.20; Found, C, 5.51; H, 1.81; N, 1.28. $Dy_{0.4}Er_{0.6}$-POM: selected IR (KBr, cm^{-1}): 3450 (br), 3039 (w), 1619 (s), 1485 (s), 1101 (s), 1049 (s), 952 (s), 890 (s), 817 (s) and 718 (w); elemental analyses (%): Calcd, C, 5.47; H, 1.96; N, 1.20; Found, C, 5.50; H, 1.87; N, 1.29. $Dy_{0.3}Er_{0.7}$-POM: selected IR (KBr, cm^{-1}): 3447 (br), 3042 (w), 1619 (s), 1485 (s), 1104 (s), 1050 (s), 953 (s), 892 (s), 820 (s) and 721 (w); elemental analyses (%): Calcd, C, 5.47; H, 1.96; N, 1.20; Found, C, 5.54; H, 1.86; N, 1.33. $Dy_{0.2}Er_{0.8}$-POM: selected IR (KBr, cm^{-1}): 3449 (br), 3042 (w), 1621 (s), 1486 (s), 1094 (s), 1048 (s), 952 (s), 888 (s), 829 (s) and 718 (w); elemental analyses (%): Calcd, C, 5.47; H, 1.96; N, 1.20; Found, C, 5.53; H, 1.79; N, 1.32. $Dy_{0.1}Er_{0.9}$-POM: selected IR (KBr, cm^{-1}): 3447 (br), 3038 (w), 1624 (s), 1486 (s), 1095 (s), 1049 (s), 952 (s), 888 (s), 824 (s) and 717 (w); elemental analyses (%): Calcd, C, 5.47; H, 1.96; N, 1.20; Found, C, 5.55; H, 1.67; N, 1.25.

RESULTS AND DISCUSSION

IR Spectra. Figure 1a shows the IR spectra of $Dy_xEr_{(1-x)}$-POM (x = 0−1). All samples have similar characteristic peaks recorded from 4000 to 400 cm^{-1}. The characteristic peaks at 1100 to 700 cm^{-1} can be attributed to the $\nu(P-O_a)$, $\nu(W-O_t)$, $\nu(W-O_b)$, and $\nu(W-O_c)$ vibrations of the $\{PW_{11}\}$ skeleton in $Dy_xEr_{(1-x)}$-POM. The vibration absorption peaks at around 3040 and 1620 cm^{-1} can be assigned to $\nu(C-H)$ and $\nu(C=O)$ stretching vibrations. The strong absorption band at around 1486 cm^{-1} is a positive signature of the $\nu(C-N)$ stretching vibration of $[(CH_3)_4N]^+$ countercations. The broad band located around 3450 cm^{-1} is due to the stretching vibration of lattice water molecules.

Powder X-ray Diffraction. The PXRD patterns of $Dy_xEr_{(1-x)}$-POM samples were recorded at room temperature as shown in Figure 1b. The diffraction signals of $Dy_xEr_{(1-x)}$-POM samples are in good agreement with the reported Dy-POM, and no obvious changes were observed in the crystal structure when Dy^{3+} ions were partially replaced by Er^{3+} ions. It

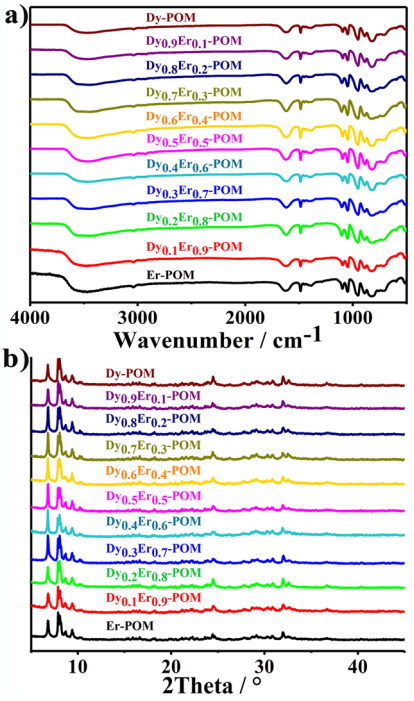

Figure 1. (a) IR spectra of $Dy_xEr_{(1-x)}$-POM (x = 0−1); (b) PXRD patterns of $Dy_xEr_{(1-x)}$-POM.

should also be noted that no noticeable shift could be seen in the diffraction signals even when most of Er^{3+} ions were replaced by Dy^{3+} ions (90%) in their crystal lattice, which can be ascribed to the similar ionic radii and coordination geometries of Er^{3+} and Dy^{3+} ions that thus results in isomorphic $Dy_xEr_{(1-x)}$-POM derivatives.

Crystallographic Parameters. As shown in Table S2, $Dy_xEr_{(1-x)}$-POM have similar crystallographic parameters, which are in good agreement with the results of IR and PXRD. The negligible crystal lattice distortion for $Dy_xEr_{(1-x)}$-POM samples may not cause obvious shift in their diffraction peaks, thus there is no hindrance for the insertion of different Ln^{3+} ions into the POMs skeleton. All these investigations show that the Er^{3+}-doped $Dy_xEr_{(1-x)}$-POM samples are isomorphic with single component Dy-POM.

Structural Description. The PXRD patterns and crystallographic parameters of samples were investigated to affirm the structural similarity in $Dy_xEr_{(1-x)}$-POM, which crystallizes in orthorhombic space group $Pna2_1$. Herein, the structural description of Dy-POM was described in detail. Dy-POM is comprised of one fundamental dimeric polyanion skeleton $[Dy(C_4H_2O_6)(\alpha\text{-}PW_{11}O_{39})]_2^{16-}$, three K^+ cations, six $[N(CH_3)_4]^{3+}$ countercations, and 27 lattice water molecules, and simultaneously seven protons are directly added for charge balance of negative polyanion.[42] The addition of protons is very consistent with the acidic reaction environment (pH = 3.2). As shown in Figure 2a, the dimeric $[Dy(C_4H_2O_6)(\alpha\text{-}PW_{11}O_{39})]_2^{16-}$ polyanion can be regarded as two monolacunary Keggin-type $[\alpha\text{-}PW_{11}O_{39}]^{7-}$ fragments linked by the organic−inorganic hybrid species $[Dy(C_4H_2O_6)]_2^{2-}$. The $[Dy(C_4H_2O_6)]_2^{2-}$ species can be seen as two Dy^{3+} ions chelated by two tartrate ligands through one O atom from carboxyl group and one O atom from hydroxyl group of each tartrate ligand (Figure 2b). Two $[\alpha\text{-}PW_{11}O_{39}]^{7-}$ fragments originate from the decomposition of $[P_2W_{19}O_{69}(H_2O)]^{14-}$ precursor in

DOI: 10.1021/acs.inorgchem.8b00674
Inorg. Chem. 2018, 57, 7665−7675

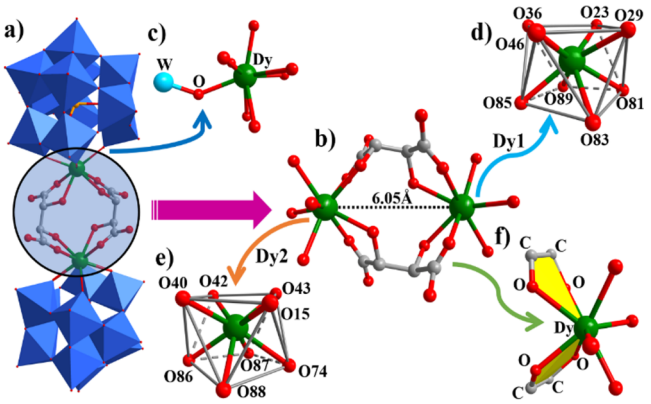

Figure 2. (a) Combined polyhedral/ball-and-stick representation of polyanion for Dy-POM; (b) coordination mode of Dy^{3+} ions and tartarate ligands; (c) angle of Dy−O−W; (d) coordination environment of Dy1 ion; (e) coordination environment of Dy2 ion; (f) five-membered Dy−O−C−C−O rings constructed by coordination of tartarate ligands and Dy^{3+} ions (color code: WO_6, blue; W, turquoise; P, light orange; Dy, green; O, red; C, gray).

an acidic reaction environment. The $[Dy(C_4H_2O_6)]_2^{2-}$ segment and two $[\alpha\text{-}PW_{11}O_{39}]^{7-}$ fragments are connected with each other by Dy^{3+} ions into the defect site of $[PW_{11}O_{39}]^{7-}$ with the angles of Ln−O−W in the range of 135.330(14)−158.495(14)° (the average angle is 146.608(15)) (Figure 2c). Both Dy^{3+} ions in $[Dy(C_4H_2O_6)(\alpha\text{-}PW_{11}O_{39})]_2^{16-}$ polyanion display 8-fold coordination distorted square antiprism configurations, which are constructed by four O atoms from each monolacunary Keggin $[\alpha\text{-}PW_{11}O_{39}]^{7-}$ and from two tartrate ligands. Specifically, the Dy1 atom is 8-fold coordinated by four O atoms (O23, O29, 036, and O46) from $[\alpha\text{-}PW_{11}O_{39}]^{7-}$ subunit and another from two tartrate ligands (O81, O83, 085, and O89), which can be anticipated for a distorted square antiprism geometry with Dy1−O bond lengths of 2.32(3)−2.52(3) Å and O−Dy1−O angles of 64.6(12)−148.3(11)° (Figure 2d). In contrast, the square antiprism geometry of Dy2 atom is constructed by four O atoms (O15, O40, 042, and O43) from another $[\alpha\text{-}PW_{11}O_{39}]^{7-}$ subunit and four O atoms (O74, O86, 087, and O88) from two tartrate ligands with Dy2−O bond lengths of 2.29(3)−2.46(3) Å and O−Dy2−O angles of 63.1(13)−146.9(12)° (Figure 2e). In addition, the distance between Dy1 and Dy2 atoms in dimeric $[Dy(C_4H_2O_6)(\alpha\text{-}PW_{11}O_{39})]_2^{16-}$ polyanion is 6.05(2) Å. Interestingly, the tartrate ligands take part in the construction of a $[Dy(C_4H_2O_6)(\alpha\text{-}PW_{11}O_{39})]_2^{16-}$ skeleton through the formation of five-member Dy−O−C−C−O chelate rings (Figure 2f), which play a crucial role in stabilization of the integral skeleton. It can be concluded that tartrate ligands can play an important role in the formation and stabilization of the structural units in this system.

Photoluminescence Properties. The PL of Dy^{3+} ions has been investigated primarily because of their potential applications in lighting materials, and second, the active Dy^{3+} ions can emit blue ($^4F_{9/2} \rightarrow {}^6H_{15/2}$ transition), yellow ($^4F_{9/2} \rightarrow {}^6H_{13/2}$ transition), and red ($^4F_{9/2} \rightarrow {}^6H_{11/2}$ transition) emissions in the visible area.[50−52] However, the applications of Dy^{3+}-doped materials have already been limited due to their smaller molar absorption coefficients and their tendency to exhibit different chemical environments in their surroundings. Therefore, there must be some hosts or matrix to sensitize Dy^{3+} ions to induce the characteristic emissions in such compounds. POMs can be seen as an appropriate candidate to be used as a sensitizer, as upon photoexcitation they act as antenna ligands to transfer energy from the O → M LMCT state within Ln-POMs.[53] H_2O molecules, as inorganic ligands, usually coordinate to Ln^{3+} ions in the Ln-POM complex, which can result in luminescence quenching due to coupled frequency with O−H groups oscillators. In $Dy_xEr_{(1-x)}$-POM, Ln^{3+} ions are coordinated by four O atoms from two tartrate ligands and another four O atoms from $[\alpha\text{-}PW_{11}O_{39}]^{7-}$ fragments, and hence there are no obvious O−H frequency oscillators impairing the emission of Ln^{3+} ions in $Dy_xEr_{(1-x)}$-POM. In addition, the luminescence quenching can be also operated by the hopping of d^1 electrons to Ln^{3+} ions because of fπ−pπ−dπ (Ln−O−W) orbital mixing in Ln-POM complexes. It is noteworthy to say that when the angles of Ln−O−W are around 150°, the fπ−pπ−dπ orbital mixing and electron delocalization to the similar dπ−pπ−dπ (W−O−W) can be easily overtuned. On the contrary, orbital mixing is not supported when the angles are larger or smaller than the ideal 150°.[54,55] In $Dy_xEr_{(1-x)}$-POM, the Ln−O−W bond angles can be defined in two categories: Dy−O_x−W (O_x = O15, O23, O36, O40) bond angles in the range of 135.330(14)−138.424(15)° and Dy−O_y−W (O_y = O29, O42, O43, O46) of 153.206(15)−158.495(14)°. Thus, the fπ−pπ−dπ orbital

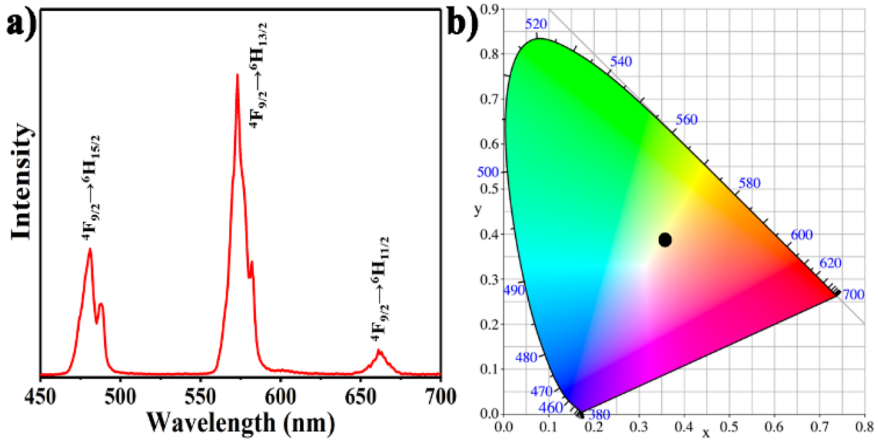

Figure 3. (a) PL emission spectra of Dy-POM powder sample (λ_{ex} = 367 nm); (b) the CIE 1931 chromaticity coordinates corresponding to the PL emission spectra of Dy-POM.

DOI: 10.1021/acs.inorgchem.8b00674
Inorg. Chem. 2018, 57, 7665−7675

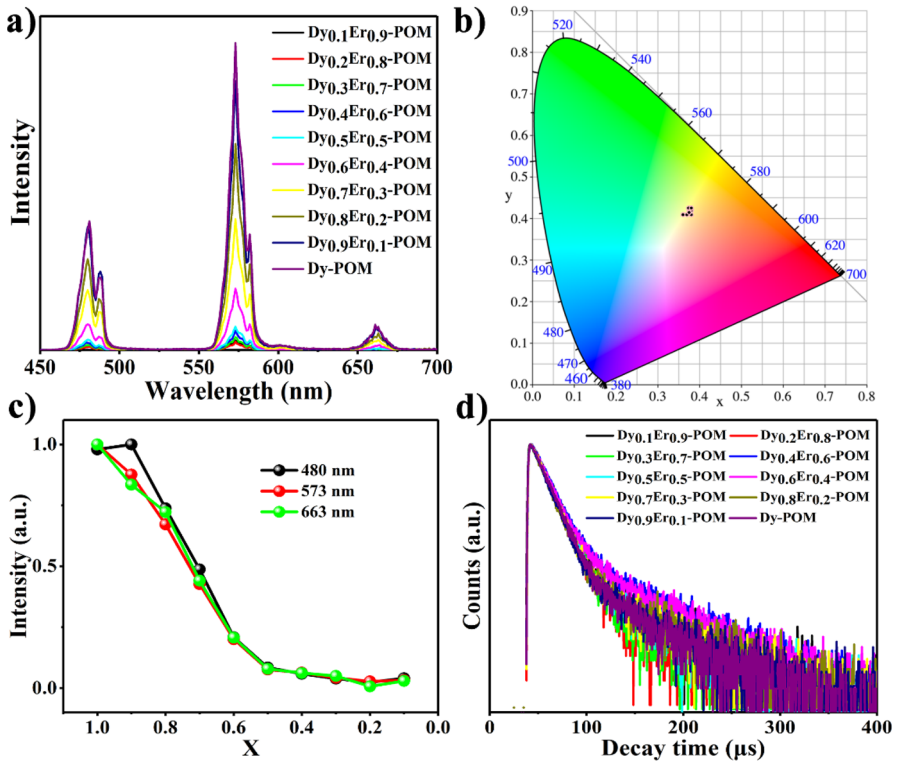

Figure 4. (a) PL emission spectra of $Dy_xEr_{(1-x)}$-POM powder sample (λ_{ex} = 367 nm); (b) the CIE 1931 chromaticity coordinates corresponding to the PL spectra of $Dy_xEr_{(1-x)}$-POM; (c) corresponding line charts of emission intensity at 480, 573, and 663 nm of $Dy_xEr_{(1-x)}$-POM; (d) PL decay time diagrams of $Dy_xEr_{(1-x)}$-POM powder sample upon excitation at 367 nm and emission at 573 nm. Note that x in $Dy_xEr_{(1-x)}$-POM is 0.1−1.

mixing cannot effectively give rise to luminescence quenching in $Dy_xEr_{(1-x)}$-POM.

As shown in Figure 3a, the characteristic emission peaks of Dy-POM upon excitation of 367 nm appearing at 480, 573, and 663 nm are indicative of $^4F_{9/2} \rightarrow {}^6H_{15/2}$, $^4F_{9/2} \rightarrow {}^6H_{13/2}$, and $^4F_{9/2} \rightarrow {}^6H_{11/2}$ transitions, respectively. The emissions at 480 and 573 nm split up into two peaks due to lower symmetry with no inversion center on the emitting atoms, which is very consistent with the crystal structure. Obviously, the blue (480 nm) and yellow (573 nm) emissions are dominated in the spectrum, and the CIE 1931 chromaticity coordinates (0.38, 0.43) are located in near-white light (Figure 3b). Especially, the highest intensity of the electric dipole $^4F_{9/2} \rightarrow {}^6H_{13/2}$ transition strongly depends on the local environment prevailing in Dy^{3+} ions,[56,57] yet the magnetic dipole $^4F_{9/2} \rightarrow {}^6H_{13/2}$ transition is insensitive to the crystal field effects and local environment around Dy^{3+} ions. Obviously, the emission intensity of electric dipole $^4F_{9/2} \rightarrow {}^6H_{13/2}$ transition is much higher than the magnetic dipole $^4F_{9/2} \rightarrow {}^6H_{15/2}$ transition. The PL emission spectra, CIE 1931 chromaticity coordinates, line charts of emission intensity, and decay time curves of $Dy_xEr_{(1-x)}$-POM samples are illustrated in Figure 4, and PL excitation spectra are shown in Figure S4. The room temperature PL emission spectra of $Dy_xEr_{(1-x)}$-POM are investigated to demonstrate any influence in their emission characteristics and optical quality on different Er^{3+}-doping concentrations (Figure 4a). For $Dy_xEr_{(1-x)}$-POM, the PL emission intensity gradually decreases as the value of x decreases. As a result, when the Er^{3+}-doping concentration reaches 20%, the emission intensity drops to ~75% as compared to that of Dy-POM. At high Er^{3+}-doping concentration (x is less than 0.5), the emission intensity of Dy^{3+} emitting center drops to ~5% of the emission intensity of Dy-POM (Figure 4c). However, no noticeable shift in the characteristic emissions is observed (480, 573, and 663 nm) in the spectra. Surprisingly, no characteristic emissions of Er^{3+} ions appeared even after the increase in Er^{3+} ions to 90 percent, which may be due to inherently weak emissions of the active Er^{3+} ion even weaker by several orders of magnitude to those of the Dy^{3+} ion with a much shorter PL lifetime.[58]

The 1931 chromaticity coordinates, dominant wavelength, color purity, and CCT are important optical parameters in the process of the research of luminescent materials. The CCT can be calculated by eq 1 proposed by McCamy et al.:[59]

$$CCT = 499.0n^3 + 3525.0n^2 + 6823.3n + 5520.22 \quad (1)$$

$$n = \frac{x - x_e}{y_e - y}$$

x_e = 0.3320; y_e = 0.1858.

As shown in Table 1, the similar optical parameters prove that different Er^{3+} concentration doped $Dy_xEr_{(1-x)}$-POM samples have a similar optical property except for emission intensity, which can be attributed to the dominant of Dy^{3+} ion emission in the samples (Figure 4b). The decay time curves of $Dy_xEr_{(1-x)}$-POM samples upon excitation at 367 nm and emission at 573 nm are shown in Figure 4d, and the decay time can be fitted by the following double exponential function:[60]

$$I(t) = \alpha_1 e^{(1/\tau_1)} + \alpha_2 e(t/\tau_2) \quad (2)$$

where $I(t)$ is the emission intensity at time t, $\alpha_1 + \alpha_2 = 1$, α_1 and α_2 are the fractional contributions of lifetime τ_1 and τ_2, τ_1 represents the short time component, and τ_2 represents the long time component.

DOI: 10.1021/acs.inorgchem.8b00674
Inorg. Chem. 2018, 57, 7665−7675

Table 1. Optical Parameters of $Dy_xEr_{(1-x)}$-POM Samples upon Excitation Wavelength at 367 nm (x = 0.1−1) and 380 nm (x = 0)

sample	CIE 1931 coordinates (x, y)	dominant wavelength (nm)	color purity (%)	T_{cp} (K)
$Dy_{0.1}Er_{0.9}$-POM	0.36, 0.41	566	32.69	4703
$Dy_{0.2}Er_{0.8}$-POM	0.37, 0.41	570	36.87	4373
$Dy_{0.3}Er_{0.7}$-POM	0.38, 0.43	570	42.64	4254
$Dy_{0.4}Er_{0.6}$-POM	0.38, 0.42	570	38.99	4327
$Dy_{0.5}Er_{0.5}$-POM	0.38, 0.42	570	41.30	4296
$Dy_{0.6}Er_{0.4}$-POM	0.38, 0.42	570	40.48	4307
$Dy_{0.7}Er_{0.3}$-POM	0.38, 0.43	570	42.88	4248
$Dy_{0.8}Er_{0.2}$-POM	0.38, 0.43	570	41.69	4290
$Dy_{0.9}Er_{0.1}$-POM	0.36, 0.40	567	29.07	4724
Dy-POM	0.38, 0.43	570	43.35	4263
Er-POM	0.47, 0.52	574	98.50	3264

The fitting results of $Dy_xEr_{(1-x)}$-POM are shown in Table 2. The values of τ_1 and τ_2 gradually increase with the increase in doped Er^{3+} concentration.

Table 2. Biexponential Fitting Results of $Dy_xEr_{(1-x)}$-POM (x = 0.1−1) Samples upon Excitation at 367 nm and Emission at 573 nm and Er-POM Sample upon Excitation at 380 nm and Emission at 554 nm

sample	τ_1 (μs)	α_1 (%)	τ_2 (μs)	α_2 (%)
$Dy_{0.1}Er_{0.9}$-POM	15.57	86.93	85.63	13.07
$Dy_{0.2}Er_{0.8}$-POM	15.84	47.59	81.87	52.41
$Dy_{0.3}Er_{0.7}$-POM	15.77	96.04	83.24	3.96
$Dy_{0.4}Er_{0.6}$-POM	14.95	80.52	80.74	19.48
$Dy_{0.5}Er_{0.5}$-POM	14.64	92.42	81.36	7.58
$Dy_{0.6}Er_{0.4}$-POM	15.10	71.20	78.92	28.80
$Dy_{0.7}Er_{0.3}$-POM	14.65	81.12	76.66	18.88
$Dy_{0.8}Er_{0.2}$-POM	14.46	76.82	79.82	23.18
$Dy_{0.9}Er_{0.1}$-POM	14.25	89.39	78.67	10.61
Dy-POM	13.68	87.48	77.84	12.52
Er-POM	2.51	30.81	11.10	69.19

The 3D EEMs of $Dy_xEr_{(1-x)}$-POM powder samples are shown in Figure 5, Figures S5 and S6. Through the EEMs of Dy-POM (Figure 5a), $Dy_{0.9}Er_{0.1}$-POM (Figure 5b), and $Dy_{0.8}Er_{0.2}$-POM (Figure 5c), it can also indicate that the emission intensity of low concentration of Er^{3+} ions doped $Dy_xEr_{(1-x)}$-POM remains stable compared to that of pure Dy-POM. The PL emission intensity of Er-POM seems to be negligible compared to that of Dy-POM under the same conditions (Figure S6), which also explain the reason for not detecting any characteristic emissions of Er^{3+} ions in PL emission spectra of $Dy_xEr_{(1-x)}$-POM (x = 0.1−1). There is no appreciable shift in excitation or emission peaks of $Dy_xEr_{(1-x)}$-POM observed in EEMs with nearly invariable optical parameters (Figures S7 and S8 and Table S3), which indicates that the dopant of Er^{3+} ions cannot effectively affect the crystal structure and emissions of Dy^{3+} ions in $Dy_xEr_{(1-x)}$-POM.

As shown in Figure S9, PL photographs of Dy-POM (Figure S9a), $Dy_{0.9}Er_{0.1}$-POM (Figure S9b), and $Dy_{0.8}Er_{0.2}$-POM (Figure S9c) were taken under different excitation wavelengths from 420 to 460 nm that are close to the commercial blue LED chip light.[61−63] $Dy_xEr_{(1-x)}$-POM (x = 0.8−1) absorbed partial energy when excited by blue light, and thus immediately emitted yellow-white light, probably due to the mixing of blue and yellow-white light, and the blue light is covered into a white light. Thus, the macroscopic white light indicates that low concentration Er^{3+} doped $Dy_xEr_{(1-x)}$-POM complexes can be potentially regarded as lighting materials covering the blue LED chip in practical applications.

Energy Transfer Mechanism. Figure 6a shows the possible process of energy transfer from POM to Dy^{3+}/Er^{3+} ions and between Er^{3+} ion and Dy^{3+} ion in $Dy_xEr_{(1-x)}$-POM. Some significant information can be acquired from the spectral layouts. First, the POM acting as a sensitizer can be excited from ground state $^1A_{1g}$ to $^1T_{1u}$ triplet state and subsequently return to the $^3T_{1u}$ triplet state through fast nonradiative transition, which is usually termed multiphonon emission.[64] Second, the photoexcitation O → M (W) LMCT $^3T_{1u}$ triplet state of POM transfers energy to the $^4S_{3/2}$ level of Er^{3+} ion and $^4F_{9/2}$ level of Dy^{3+} ion via an antenna effect. Finally, the Dy^{3+} ion emits three characteristic emissions at 480, 573, and 663 nm, whereas the Er^{3+} ion emits two characteristic emissions at 532 and 554 nm with the help of nonradiative transition. Moreover, the energy transfer could also be observed from $^4S_{3/2}$ of the Er^{3+} ion to $^4F_{9/2}$ level of the Dy^{3+} ion. To confirm this mechanism, time-resolved emission spectroscopy of the $Dy_xEr_{(1-x)}$-POM powder sample was performed under an excitation wavelength of 367 nm at room temperature. As shown in Figure 6b, Figures S10 and S11, the energy transfer process from phosphotungstate components to Dy^{3+} and Er^{3+} ions can be detected from time-resolved emission spectroscopy. First of all, the emissions at 470 and 480 nm appear at 37 μs, and it is obvious that the peak at 470 nm is prominent in the spectrum (Figure 6b). To explore the origin of the emission at 470 nm, the emission spectrum of $K_{14}[P_2W_{19}O_{69}(H_2O)]\cdot 24H_2O$ was recorded under 367 nm, which shows an emission signal at 475 nm (Figure S12). Apparently, the emission appearing at 470 nm in the time-resolved emission spectroscopy may be arising from $^3T_{1u}$ → $^1A_{1g}$ transition originating from the O → M LMCT triplet state in phosphotungstate components. As the time elapsed, the intensity of emission at 470 and 480 nm gradually increased, and the emission at 532, 554, and 573 nm appeared at 38 μs. At 38 μs, the peak at 480 nm becomes more prominent, whereas the relative emission intensity at 470 nm observed with decline intensity. Meanwhile, the emission at 663 nm appears at 39 μs. The intensity of emissions at 480, 532, and 554 nm reached a maximum at 40 μs and subsequently dropped down. Yet the intensity of emissions at 573 and 663 nm reached a maximum at 41 μs and then declined. It can be found that the characteristic emissions of Er^{3+} ion decline much faster than that of Dy^{3+} ion, which can be attributed to the much shorter PL lifetime than that of the Dy^{3+} ion.[42] Similar processes of spectral temporal evolution were detected for $Dy_xEr_{(1-x)}$-POM (x = 0.2−0.9), which exhibit the observed time-resolved emission peaks with complex kinetics. The $^4F_{9/2}$ → $^6H_{15/2}$ transition energy gap ($20.83 \times 10^3 cm^{-1}$) of the Dy^{3+} ion and $^4S_{3/2}$ → $^4I_{15/2}$ transition energy gap ($18.79 \times 10^3 cm^{-1}$) of the Er^{3+} ion are close to the energy of the $^3T_{1u}$ triplet state ($21.27 \times 10^3 cm^{-1}$) (Table 3). The calculated results reasonably approve that the photoexcitation O → M

DOI: 10.1021/acs.inorgchem.8b00674
Inorg. Chem. 2018, 57, 7665−7675

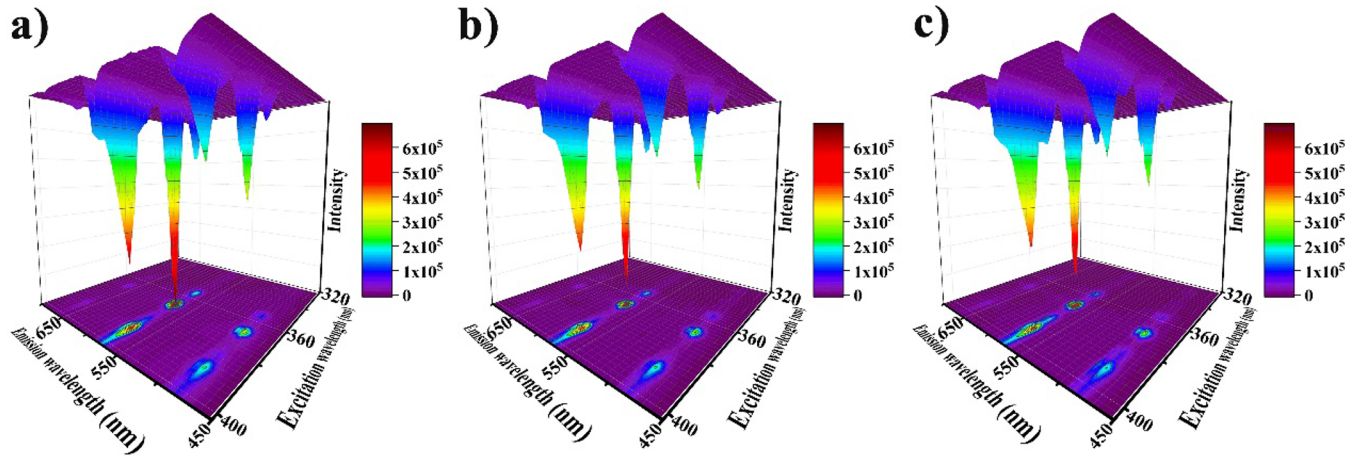

Figure 5. 3D color surface plots (top) and corresponding 2D diagrams (bottom) of luminescence excitation and emission maps (EEMs) of Dy-POM (a), $Dy_{0.9}Er_{0.1}$-POM (b), and $Dy_{0.8}Er_{0.2}$-POM (c) under the same conditions.

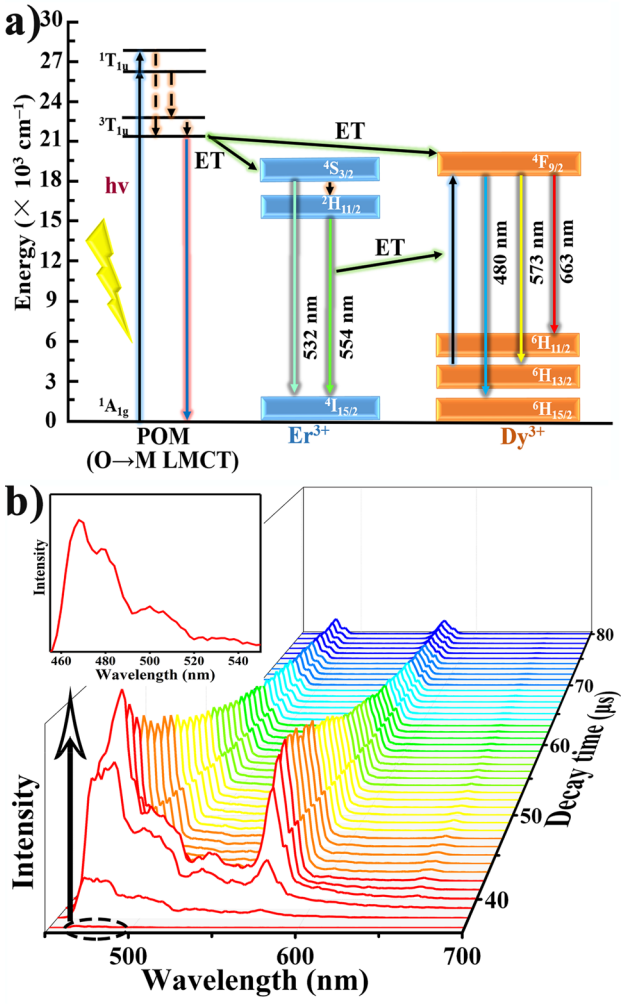

Figure 6. (a) The schematic energy level diagram demonstrating energy transfer (ET) process from POM to Dy^{3+}/Er^{3+} ions and characteristic emissions of Dy^{3+} and Er^{3+} ions (dotted line denotes nonradiative transition); (b) the time-resolved emission spectroscopy of $Dy_{0.1}Er_{0.9}$-POM powder sample under excitation wavelength at 367 nm (inset shows emission spectrum from 455 to 550 nm at 37 μs).

LMCT triplet state of phosphotungstate components can effectively sensitize the emission of Dy^{3+} and Er^{3+} ions via intramolecular energy transitions in $Dy_xEr_{(1-x)}$-POM. Moreover, the increased PL lifetime of $Dy_xEr_{(1-x)}$-POM with the increasing of Er^{3+} ions doped concentration indicates the presence of energy transfer from the Er^{3+} ion to the Dy^{3+} ion that is very consistent with closed energy gaps between the $^2H_{11/2} \rightarrow {}^4I_{15/2}$ transition ($18.05 \times 10^3 cm^{-1}$) and $^4F_{9/2} \rightarrow {}^6H_{13/2}$ transition ($17.45 \times 10^3 cm^{-1}$) (Table 2 and Table 3).[52,65]

Table 3. Calculated Energy of Different Transitions of States

transitions of states	wavelength (nm)	energy gap ($\times 10^3 cm^{-1}$)
$^3T_{1u} \rightarrow {}^1A_{1g}$	470	21.27
$^4F_{9/2} \rightarrow {}^6H_{15/2}$	480	20.83
$^4S_{3/2} \rightarrow {}^4I_{15/2}$	532	18.79
$^2H_{11/2} \rightarrow {}^4I_{15/2}$	554	18.05
$^4F_{9/2} \rightarrow {}^6H_{13/2}$	573	17.45
$^4F_{9/2} \rightarrow {}^6H_{11/2}$	663	15.08

Photostability of Luminescence. Luminescence stability plays a vital role for practical application; hence the photostability of $Dy_xEr_{(1-x)}$-POM powder samples has been further investigated. As shown in Figure 7a and Figure S13, the PL emission and excitation intensity of Dy-POM sample gradually decrease with the increase of irradiation time. The relative PL intensity at 573 nm drops to 32% of initial intensity under UV irradiation for 300 min (Figure 7b). The reason for this quenching phenomenon may be ascribed to severe photobleaching or the absorption around 605 nm of $W^V \rightarrow W^{VI}$ intervalence charge-transfer (IVCT) under irradiation.[66] In addition, Figure 7c shows the decay curves of Dy-POM upon excitation at 367 nm and emission at 573 nm with the similar profiles at different irradiation times, and the lifetime can be fitted as biexponential functions. The lifetime τ_1 and τ_2 of Dy-POM sample is shortened by increasing irradiation time. As the irradiation time increased, the values of τ_1 and τ_2 decreased from ~14 and ~78 μs to ~11 and ~52 μs, respectively (Table 4). For $Dy_{0.9}Er_{0.1}$-POM sample, the PL emission intensity also decreases as the irradiation time increased (Figure 7d). The relative emission intensity at 573 nm nearly unchanged in 15 min of irradiation, and the intensity drops to 53% of the original intensity even after 300 min of irradiation (Figure 7e). For the lifetime τ_1 and τ_2 of $Dy_{0.9}Er_{0.1}$-POM sample, the values of τ_1 remains unchanged (~14 μs) and τ_2 values decrease from ~79 μs to ~43 μs within the irradiation time from 0 to 300 min

DOI: 10.1021/acs.inorgchem.8b00674
Inorg. Chem. 2018, 57, 7665−7675

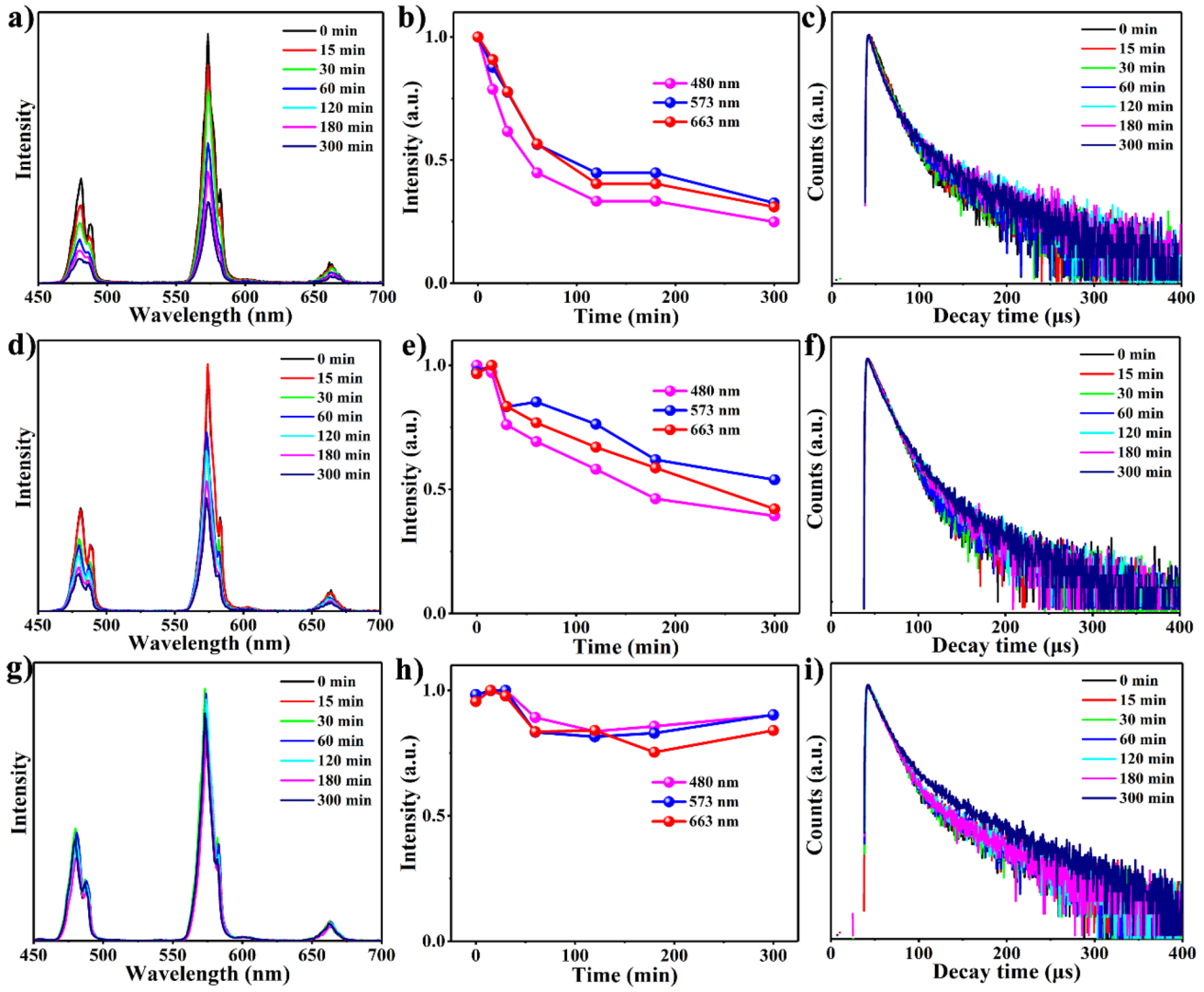

Figure 7. PL emission spectra (λ_{ex} = 367 nm) of Dy-POM (a), $Dy_{0.9}Er_{0.1}$-POM (d), and $Dy_{0.8}Er_{0.2}$-POM (g), corresponding variation rules of emission intensity at 480, 573, and 663 nm of Dy-POM (b), $Dy_{0.9}Er_{0.1}$-POM (e), and $Dy_{0.8}Er_{0.2}$-POM (h), and decay time diagrams of Dy-POM (c), $Dy_{0.9}Er_{0.1}$-POM (f), and $Dy_{0.8}Er_{0.2}$-POM (i) upon excitation at 367 nm and emission at 573 nm under continuous UV irradiation (300 W xenon lamp) for 300 min.

Table 4. Biexponential Fitting Results of Decay Time Curves of Dy-POM, $Dy_{0.9}Er_{0.1}$-POM, and $Dy_{0.8}Er_{0.2}$-POM upon Excitation at 367 nm and Emission at 573 nm under Continuous UV Irradiation (300 W Xenon Lamp) for 300 min

	Dy-POM				$Dy_{0.9}Er_{0.1}$-POM				$Dy_{0.8}Er_{0.2}$-POM			
irradiation time (min)	τ_1 (μs)	α_1 (%)	τ_2 (μs)	α_2 (%)	τ_1 (μs)	α_1 (%)	τ_2 (μs)	α_2 (%)	τ_1 (μs)	α_1 (%)	τ_2 (μs)	α_2 (%)
0	13.68	87.48	77.84	12.52	14.25	89.39	78.67	10.61	14.46	76.82	79.82	23.18
15	13.22	83.08	68.68	16.92	14.20	89.17	75.96	10.83	14.64	77.67	80.62	22.33
30	12.89	81.11	63.82	18.89	14.96	93.17	74.18	6.83	14.63	80.28	78.94	19.72
60	11.94	73.71	63.23	26.29	14.94	93.18	73.31	6.82	14.44	73.57	73.07	26.43
120	11.57	68.49	60.17	31.51	14.81	85.15	51.77	14.85	14.90	75.31	69.83	24.69
180	11.23	67.82	57.86	32.18	14.09	76.58	43.57	23.42	14.77	75.76	67.72	24.24
300	11.18	66.19	51.72	33.81	13.64	72.88	42.52	27.12	14.79	59.56	68.11	40.44

(Table 4). It is obvious that the decline of PL intensity of $Dy_{0.8}Er_{0.2}$-POM sample is less than those of Dy-POM and $Dy_{0.9}Er_{0.1}$-POM under UV irradiation (Figure 7g). The relative PL emission intensity of $Dy_{0.8}Er_{0.2}$-POM appears the same in 30 min of irradiation, and the intensity strength is up to ~85% as compared to those at 300 min of irradiation (Figure 7h). The τ_1 value of $Dy_{0.8}Er_{0.2}$-POM is approximately constant with ~14 μs, and τ_2 deceases from ~80 μs to ~68 μs as the UV irradiation time increased (Table 4). In addition, the optical parameters of $Dy_{0.8}Er_{0.2}$-POM are similar as those of both Dy-POM and $Dy_{0.9}Er_{0.1}$-POM (Table S4). It can be found that the luminescence properties of $Dy_xEr_{(1-x)}$-POM samples could maintain photostability with the decreasing value of x under consecutive UV irradiation condition (Figures S14−S23 and Tables S5 and S6). Especially, the relative PL emission intensity of Er-POM could remain above 90% of the original intensity

DOI: 10.1021/acs.inorgchem.8b00674
Inorg. Chem. 2018, 57, 7665−7675

after 300 min of UV irradiation. Most of all, $Dy_{0.8}Er_{0.2}$-POM can preserve high emission intensity and stable PL properties during 300 min of UV irradiation.

CONCLUSION

In summary, a series of $[N(CH_3)_4]_6K_3H_7[Dy_xEr_{(1-x)}(C_4H_2O_6)\text{-}(\alpha\text{-}PW_{11}O_{39})]_2\cdot 27H_2O$ (x = 0−1) ($Dy_xEr_{(1-x)}$-POM) samples were successfully prepared, which have been characterized by PXRD, TGA, ICP-AES, EDX, and IR spectra. The investigation of Ln−O−W angles indicates that the $f\pi-p\pi-d\pi$ orbital mixing cannot effectively leads to luminescence quenching. Time resolved emission spectroscopy reasonably approves the process of energy transfer in $Dy_xEr_{(1-x)}$-POM, indicating that the photoexcitation O → M LMCT state of phosphotungstate fragments can effectively sensitize the emission of Er^{3+} and Dy^{3+} ions via intramolecular energy transitions, and the energy can transfer from the Er^{3+} ion to Dy^{3+} ion. The photostability study reveals that the $Dy_{0.8}Er_{0.2}$-POM sample on continuous UV irradiation can exhibit a high PL emission intensity with wonderful stability. The $Dy_xEr_{(1-x)}$-POM (x = 1, 0.9, and 0.8) samples can emit macroscopic white light under blue irradiation, implying the samples can cover the blue LED chip to emit white light in practical applications. Furthermore, this work will provide us novel thinking to explore new and practical solid state lighting materials in the field of Ln-POM complexes.

ASSOCIATED CONTENT

Supporting Information

The Supporting Information is available free of charge on the ACS Publications website at DOI: 10.1021/acs.inorgchem.8b00674.

Synthetic method for $Dy_xEr_{(1-x)}$-POM (x = 0−0.9). The ICP results (Table S1) and crystallographic parameters of $Dy_xEr_{(1-x)}$-POM (Table S2), optical parameters and lifetime of $Dy_xEr_{(1-x)}$-POM under different irradiation time (Tables S3−S6), EDX elemental spectra, TGA curves, 3D EEMs and corresponding CIE 1931 chromaticity coordinates, photographs, time-resolved emission spectroscopy of $Dy_xEr_{(1-x)}$-POM (Figures S1−S11), emission spectrum of $K_{14}[P_2W_{19}O_{69}(H_2O)]\cdot 24H_2O$ precursor (Figure S12), PL excitation, emission and corresponding CIE 1931 chromaticity coordinates, decay curves of $Dy_xEr_{(1-x)}$-POM under different irradiation time (Figures S13−S23) (PDF)

AUTHOR INFORMATION

Corresponding Authors

*(P.-T.M.) E-mail: mpt@henu.edu.cn.

*(J.-P.W.) E-mail: jpwang@henu.edu.cn.

ORCID

Jingyang Niu: 0000-0001-6526-7767

Notes

The authors declare no competing financial interest.

ACKNOWLEDGMENTS

This work was financially supported by the National Nature Science Foundation of China (21771053, 21771054, 21571050, 21573056) Natural Science Foundation of Henan Province (132300410144 and 162300410015) and Henan Province Science and Technology Attack Plan Project (182102210237).

REFERENCES

(1) Raula, M.; Gan Or, G.; Saganovich, M.; Zeiri, O.; Wang, Y.; Chierotti, M. R.; Gobetto, R.; Weinstock, I. A. Polyoxometalate Complexes of Anatase-Titanium Dioxide Cores in Water. *Angew. Chem., Int. Ed.* **2015**, *54*, 12416−12421.

(2) Zheng, Q.; Vilà-Nadal, L.; Lang, Z.; Chen, J.-J.; Long, D.-L.; Mathieson, J. S.; Poblet, J. M.; Cronin, L. Self-Sorting of Heteroanions in the Assembly of Cross-Shaped Polyoxometalate Clusters. *J. Am. Chem. Soc.* **2018**, *140*, 2595−2601.

(3) Ma, P.; Hu, F.; Wang, J.; Niu, J. Carboxylate Covalently Modified Polyoxometalates: From Synthesis, Structural Diversity to Applications. *Coord. Chem. Rev.* **2018**, DOI: 10.1016/j.ccr.2018.02.010.

(4) Miras, H. N.; Yan, J.; Long, D.-L.; Cronin, L. Engineering Polyoxometalates with Emergent Properties. *Chem. Soc. Rev.* **2012**, *41*, 7403.

(5) Parrot, A.; Bernard, A.; Jacquart, A.; Serapian, S. A.; Bo, C.; Derat, E.; Oms, O.; Dolbecq, A.; Proust, A.; Métivier, R.; et al. Photochromism and Dual-Color Fluorescence in a Polyoxometalate-Benzospiropyran Molecular Switch. *Angew. Chem., Int. Ed.* **2017**, *56*, 4872−4876.

(6) Hou, X.-S.; Zhu, G.-L.; Ren, L.-J.; Huang, Z.-H.; Zhang, R.-B.; Ungar, G.; Yan, L.-T.; Wang, W. Mesoscale Graphene-like Honeycomb Mono- and Multilayers Constructed via Self-Assembly of Coclusters. *J. Am. Chem. Soc.* **2018**, *140*, 1805−1811.

(7) Sivakumar, S.; van Veggel, F. C. J. M.; Raudsepp, M. Bright White Light through Up-Conversion of a Single NIR Source from Sol−Gel-Derived Thin Film Made with Ln^{3+}-Doped LaF_3 Nanoparticles. *J. Am. Chem. Soc.* **2005**, *127*, 12464−12465.

(8) Dai, Q.; Foley, M. E.; Breshike, C. J.; Lita, A.; Strouse, G. F. Ligand-Passivated Eu:Y_2O_3 Nanocrystals as a Phosphor for White Light Emitting Diodes. *J. Am. Chem. Soc.* **2011**, *133*, 15475−15486.

(9) Kokuoz, B.; DiMaio, J. R.; Kucera, C. J.; Evanoff, D. D.; Ballato, J. Color Kinetic Nanoparticles. *J. Am. Chem. Soc.* **2008**, *130*, 12222−12223.

(10) Wan, J.; Liu, Q.; Liu, G.; Zhou, Z.; Ni, J.; Xie, R.-J. A Novel Eu^{2+} Activated G-$La_2Si_2O_7$ Phosphor for White LEDs: SiC-Reduction Synthesis, Tunable Luminescence and Good Thermal Stability. *J. Mater. Chem. C* **2017**, *5*, 1614−1623.

(11) Lin, C. C.; Xiao, Z. R.; Guo, G.-Y.; Chan, T.-S.; Liu, R.-S. Versatile Phosphate Phosphors $ABPO_4$ in White Light-Emitting Diodes: Collocated Characteristic Analysis and Theoretical Calculations. *J. Am. Chem. Soc.* **2010**, *132*, 3020−3028.

(12) Lv, Y.; Wang, L.; Zhuang, Y.; Zhou, T.-L.; Xie, R.-J. Discovery of the Yb^{2+}−Yb^{3+} Couple as Red-to-NIR Persistent Luminescence Emitters in Yb-Activated $(Ba_{1-x}Sr_x)AlSi_5O_2N_7$ Phosphors. *J. Mater. Chem. C* **2017**, *5*, 7095−7101.

(13) Li, S.; Zhu, Q.; Tang, D.; Liu, X.; Ouyang, G.; Cao, L.; Hirosaki, N.; Nishimura, T.; Huang, Z.; Xie, R.-J. Al_2O_3−YAG:Ce Composite Phosphor Ceramic: A Thermally Robust and Efficient Color Converter for Solid State Laser Lighting. *J. Mater. Chem. C* **2016**, *4*, 8648−8654.

(14) Lei, F.; Yan, B. Hydrothermal Synthesis and Luminescence of CaMO4:RE^{3+} (M = W, Mo; RE = Eu, Tb) Submicro-Phosphors. *J. Solid State Chem.* **2008**, *181*, 855−862.

(15) Ahmed, Z.; Aderne, R. E.; Kai, J.; Chavarria, H. I. P.; Cremona, M. Cremona, M. Ytterbium β-Diketonate Complexes for near Infra-Red Organic Light-Emitting Devices. *Thin Solid Films* **2016**, *620*, 34−42.

(16) Verwey, J. W. M.; Dirksen, G. J.; Blasse, G. A Study of the Charge-transfer State in Lanthanide-Borate Glasses. *J. Non-Cryst. Solids* **1988**, *107*, 49−54.

(17) Yamase, T.; Kobayashi, T.; Sugeta, M.; Naruke, H. Europium-(III) Luminescence and Intramolecular Energy Transfer Studies of Polyoxometalloeuropates. *J. Phys. Chem. A* **1997**, *101*, 5046−5053.

(18) Yamase, T. Chapter 243 Luminescence of Polyoxometallolanthanoates and Photochemical Nano-Ring Formation. In *Handbook on the Physics and Chemistry of Rare Earths*; Elsevier, 2009; Vol. *39*, pp 297−356.

DOI: 10.1021/acs.inorgchem.8b00674
Inorg. Chem. 2018, 57, 7665−7675

(19) Ahmed, Z.; Iftikhar, K. Efficient Layers of Emitting Ternary Lanthanide Complexes for Fabricating Red, Green, and Yellow OLEDs. *Inorg. Chem.* **2015**, *54*, 11209−11225.
(20) Miyata, K.; Nakagawa, T.; Kawakami, R.; Kita, Y.; Sugimoto, K.; Nakashima, T.; Harada, T.; Kawai, T.; Hasegawa, Y. Remarkable Luminescence Properties of Lanthanide Complexes with Asymmetric Dodecahedron Structures. *Chem. - Eur. J.* **2011**, *17*, 521−528.
(21) Fan, L.; Fan, W.; Li, B.; Zhao, X.; Zhang, X. W-Shaped 1,3-di(2,4-Dicarboxyphenyl) benzene Based Lanthanide Coordination Polymers with Tunable White Light Emission. *New J. Chem.* **2016**, *40*, 10440−10446.
(22) Pavani, K.; Kumar, J. S.; Sasikala, T.; Jamalaiah, B. C.; Seo, H. J.; Moorthy, L. R. Luminescent Characteristics of Dy^{3+} Doped Strontium Magnesium Aluminate Phosphor for White LEDs. *Mater. Chem. Phys.* **2011**, *129*, 292−295.
(23) Quici, S.; Marzanni, G.; Forni, A.; Accorsi, G.; Barigelletti, F. New Lanthanide Complexes for Sensitized Visible and Near-IR Light Emission: Synthesis, ^{1}H NMR, and X-Ray Structural Investigation and Photophysical Properties. *Inorg. Chem.* **2004**, *43*, 1294−1301.
(24) Peacock, R. D.; Weakley, T. J. R. Heteropolytungstate Complexes of the Lanthanide Elements. Part I. Preparation and Reactions. *J. Chem. Soc. A* **1971**, 1836−1839.
(25) Hussain, F.; Conrad, F.; Patzke, G. A Gadolinium-Bridged Polytungstoarsenate(III) Nanocluster: $[Gd_8As_{12}W_{124}O_{432}(H_2O)_{22}]^{60-}$. *Angew. Chem., Int. Ed.* **2009**, *48*, 9088−9091.
(26) Fukaya, K.; Yamase, T. Alkali-Metal-Controlled Self-Assembly of Crown-Shaped Ring Complexes of Lanthanide/$[\alpha$-$AsW_9O_{33}]^{9-}$: $[K\{Eu(H_2O)_2(\alpha$-$AsW_9O_{33})\}_6]^{35-}$ and $[Cs\{Eu(H_2O)_2(\alpha$-$AsW_9O_{33})\}_4]^{23-}$. *Angew. Chem., Int. Ed.* **2003**, *42*, 654−658.
(27) Barsukova, M.; Izarova, N. V.; Biboum, R. N.; Keita, B.; Nadjo, L.; Ramachandran, V.; Dalal, N. S.; Antonova, N. S.; Carbó, J. J.; Poblet, J. M.; et al. Polyoxopalladates Encapsulating Yttrium and Lanthanide Ions, $[X^{III}Pd^{II}_{12}(AsPh)_8O_{32}]^{5-}$ (X = Y, Pr, Nd, Sm, Eu, Gd, Tb, Dy, Ho, Er, Tm, Yb, Lu). *Chem. - Eur. J.* **2010**, *16*, 9076−9085.
(28) Ma, X.; Yang, W.; Chen, L.; Zhao, J. Significant Developments in Rare-Earth-Containing Polyoxometalate Chemistry: Synthetic Strategies, Structural Diversities and Correlative Properties. *CrystEngComm* **2015**, *17*, 8175−8197.
(29) Ritchie, C.; Moore, E. G.; Speldrich, M.; Kögerler, P.; Boskovic, C. Terbium Polyoxometalate Organic Complexes: Correlation of Structure with Luminescence Properties. *Angew. Chem., Int. Ed.* **2010**, *49*, 7702−7705.
(30) Ritchie, C.; Baslon, V.; Moore, E. G.; Reber, C.; Boskovic, C. Sensitization of Lanthanoid Luminescence by Organic and Inorganic Ligands in Lanthanoid-Organic-Polyoxometalates. *Inorg. Chem.* **2012**, *51*, 1142−1151.
(31) Liu, Y.; Li, H.; Lu, C.; Gong, P.; Ma, X.; Chen, L.; Zhao, J. Organocounterions-Assisted and pH-Controlled Self-Assembly of Five Nanoscale High-Nuclear Lanthanide Substituted Heteropolytungstates. *Cryst. Growth Des.* **2017**, *17*, 3917−3928.
(32) Li, H.; Liu, Y.; Zheng, R.; Chen, L.; Zhao, J.-W.; Yang, G.-Y. Trigonal Pyramidal $\{AsO_2(OH)\}$ Bridging Tetranuclear Rare-Earth Encapsulated Polyoxotungstate Aggregates. *Inorg. Chem.* **2016**, *55*, 3881−3893.
(33) Han, Q.; Wen, Y.; Liu, J.-C.; Zhang, W.; Chen, L.-J.; Zhao, J.-W. Rare-Earth-Incorporated Tellurotungstate Hybrids Functionalized by 2-Picolinic Acid Ligands: Syntheses, Structures, and Properties. *Inorg. Chem.* **2017**, *56*, 13228−13240.
(34) Li, H.-L.; Liu, Y.-J.; Liu, J.-L.; Chen, L.-J.; Zhao, J.-W.; Yang, G.-Y. Structural Transformation from Dimerization to Tetramerization of Serine-Decorated Rare-Earth-Incorporated Arsenotungstates Induced by the Usage of Rare-Earth Salts. *Chem. - Eur. J.* **2017**, *23*, 2673−2689.
(35) Wang, Y.; Sun, X.; Li, S.; Ma, P.; Niu, J.; Wang, J. Generation of Large Polynuclear Rare Earth Metal-Containing Organic−Inorganic Polytungstoarsenate Aggregates. *Cryst. Growth Des.* **2015**, *15*, 2057−2063.
(36) Wang, J.; Niu, Y.; Zhang, M.; Ma, P.; Zhang, C.; Niu, J.; Wang, J. Organophosphonate-Functionalized Lanthanopolyoxomolybdate: Synthesis, Characterization, Magnetism, Luminescence, and Catalysis of H_2O_2-Based Thioether Oxidation. *Inorg. Chem.* **2018**, *57*, 1796−1805.
(37) Ma, P.; Hu, F.; Huo, Y.; Zhang, D.; Zhang, C.; Niu, J.; Wang, J. Magnetoluminescent Bifunctional Dysprosium-Based Phosphotungstates with Synthesis and Correlations between Structures and Properties. *Cryst. Growth Des.* **2017**, *17*, 1947−1956.
(38) Ma, P.; Wan, R.; Wang, Y.; Hu, F.; Zhang, D.; Niu, J.; Wang, J. Coordination-Driven Self-Assembly of a 2D Graphite-Like Framework Constructed from High-Nuclear Ce_{10} Cluster Encapsulated Polyoxotungstates. *Inorg. Chem.* **2016**, *55*, 918−924.
(39) Ban, R.; Sun, X.; Wang, J.; Ma, P.; Zhang, C.; Niu, J.; Wang, J. Polyoxotungstate Incorporating Organotriphosphonate Ligands and Lanthanide Ions: Syntheses, Characterization, Magnetism and Photoluminescence Properties. *Dalton Trans.* **2017**, *46*, 5856−5863.
(40) Ma, P.; Wan, R.; Si, Y.; Hu, F.; Wang, Y.; Niu, J.; Wang, J. Double-Malate Bridging Tri-Lanthanoid Cluster Encapsulated Arsenotungstates: Syntheses, Structures, Luminescence and Magnetic Properties. *Dalton Trans.* **2015**, *44*, 11514−11523.
(41) Chen, S.; Ma, P.; Luo, H.; Wang, Y.; Niu, J.; Wang, J. A Luminescent Polyoxoniobate Lanthanide Derivative $\{Eu_3(H_2O)_9[Nb_{48}O_{138}(H_2O)_6]\}^{27-}$. *Chem. Commun.* **2017**, *53*, 3709−3712.
(42) Ma, P.; Hu, F.; Wan, R.; Huo, Y.; Zhang, D.; Niu, J.; Wang, J. Magnetic Double-Tartaric Bridging Mono-Lanthanide Substituted Phosphotungstates with Photochromic and Switchable Luminescence Properties. *J. Mater. Chem. C* **2016**, *4*, 5424−5433.
(43) Wu, H.; Wan, R.; Si, Y.; Ma, P.; Wang, J.; Niu, J. A Helical Chain-like Organic−inorganic Hybrid Arsenotungstate with Color-Tunable Photoluminescence. *Dalton Trans.* **2018**, *47*, 1958−1965.
(44) Sato, R.; Suzuki, K.; Sugawa, M.; Mizuno, N. Heterodinuclear Lanthanoid-Containing Polyoxometalates: Stepwise Synthesis and Single-Molecule Magnet Behavior. *Chem. - Eur. J.* **2013**, *19*, 12982−12990.
(45) Shiddiq, M.; Komijani, D.; Duan, Y.; Gaita-Ariño, A.; Coronado, E.; Hill, S. Enhancing Coherence in Molecular Spin Qubits via Atomic Clock Transitions. *Nature* **2016**, *531*, 348−351.
(46) Zhao, W.; Zou, C.; Shi, L.; Yu, J.; Qian, G.; Wu, C. Synthesis of diamondoid lanthanide-polyoxometalate solids as tunable photoluminescent materials. *Dalton Trans.* **2012**, *41*, 10091−10096.
(47) Kaczmarek, A. M.; Van Hecke, K.; Van Deun, R. Low-Percentage Ln^{3+} Doping in a Tetranuclear Lanthanum Polyoxometalate Assembled from $[Mo_7O_{24}]^{6-}$ Polyanions Yielding Visible and Near-Infrared Luminescence. *Inorg. Chem.* **2017**, *56*, 3190−3200.
(48) Kaczmarek, A. M.; Liu, J.; Laforce, B.; Vincze, L.; Van Hecke, K.; Van Deun, R. Cryogenic Luminescent Thermometers Based on Multinuclear Eu^{3+}/Tb^{3+} Mixed Lanthanide Polyoxometalates. *Dalton Trans.* **2017**, *46*, 5781−5785.
(49) Ji, H.; Li, X.; Xu, D.; Zhou, Y.; Zhang, L.; Zuhra, Z.; Yang, S. Synthesis, Structure, and Photoluminescence of Color-Tunable and White-Light-Emitting Lanthanide Metal−Organic Open Frameworks Composed of $AlMo_6(OH)_6O_{18}^{3-}$ Polyanion and Nicotinate. *Inorg. Chem.* **2017**, *56*, 156−166.
(50) Liu, Q.; Liu, Y.; Ding, Y.; Peng, Z.; Tian, X.; Yu, Q.; Dong, G. A White Light Emitting Luminescent Material $Ba_3Y(PO_4)_3$:Dy^{3+}. *Ceram. Int.* **2014**, *40*, 10125−10129.
(51) Liu, F.; Liu, Q.; Fang, Y.; Zhang, N.; Yang, B.; Zhao, G. White Light Emission from $NaLa(PO_3)_4$:Dy^{3+} Single-Phase Phosphors for Light-Emitting Diodes. *Ceram. Int.* **2015**, *41*, 1917−1920.
(52) Zhang, J.; Cai, G.-M.; Yang, L.-W.; Ma, Z.-Y.; Jin, Z.-P. Layered Crystal Structure, Color-Tunable Photoluminescence, and Excellent Thermal Stability of $MgIn_2P_4O_{14}$ Phosphate-Based Phosphors. *Inorg. Chem.* **2017**, *56*, 12902−12913.
(53) Ritchie, C.; Moore, E. G.; Speldrich, M.; Kögerler, P.; Boskovic, C. Terbium Polyoxometalate Organic Complexes: Correlation of Structure with Luminescence Properties. *Angew. Chem., Int. Ed.* **2010**, *49*, 7702−7705.
(54) Artetxe, B.; Reinoso, S.; San Felices, L.; Lezama, L.; Gutiérrez-Zorrilla, J. M.; García, J. A.; Galán-Mascarós, J. R.; Haider, A.; Kortz, U.; Vicent, C. Cation-Directed Dimeric versus Tetrameric Assemblies

DOI: 10.1021/acs.inorgchem.8b00674
Inorg. Chem. 2018, 57, 7665−7675

of Lanthanide-Stabilized Dilacunary Keggin Tungstogermanates. *Chem. - Eur. J.* **2014**, *20*, 12144−12156.
(55) Artetxe, B.; Reinoso, S.; San Felices, L.; Gutiérrez-Zorrilla, J. M.; García, J. A.; Haso, F.; Liu, T.; Vicent, C. Crown-Shaped Tungstogermanates as Solvent-Controlled Dual Systems in the Formation of Vesicle-Like Assemblies. *Chem. - Eur. J.* **2015**, *21*, 7736−7745.
(56) Bag, P.; Rastogi, C. K.; Biswas, S.; Sivakumar, S.; Mereacre, V.; Chandrasekhar, V. Homodinuclear Lanthanide $\{Ln_2\}$ (Ln = Gd, Tb, Dy, Eu) Complexes Prepared from an O-Vanillin Based Ligand: Luminescence and Single-Molecule Magnetism Behavior. *Dalton Trans.* **2015**, *44*, 4328−4340.
(57) Biju, S.; Gopakumar, N.; Bünzli, J.-C. G.; Scopelliti, R.; Kim, H. K.; Reddy, M. L. P. Brilliant Photoluminescence and Triboluminescence from Ternary Complexes of Dy^{III} and Tb^{III} with 3-Phenyl-4-Propanoyl-5-Isoxazolonate and a Bidentate Phosphine Oxide Coligand. *Inorg. Chem.* **2013**, *52*, 8750−8758.
(58) *Rare Earth Coordination Chemistry: Fundamentals and Applications*; Huang, C.-H., Ed.; John Wiley & Sons: Hoboken, NJ, 2010.
(59) McCamy, C. S. Correlated Color Temperature as an Explicit Function of Chromaticity Coordinates. *Color Res. Appl.* **1992**, *17*, 142−144.
(60) Li, H.-L.; Liu, Y.-J.; Liu, J.-L.; Chen, L.-J.; Zhao, J.-W.; Yang, G.-Y. Structural Transformation from Dimerization to Tetramerization of Serine-Decorated Rare-Earth-Incorporated Arsenotungstates Induced by the Usage of Rare-Earth Salts. *Chem. - Eur. J.* **2017**, *23*, 2673−2689.
(61) Li, S.; Wang, L.; Tang, D.; Cho, Y.; Liu, X.; Zhou, X.; Lu, L.; Zhang, L.; Takeda, T.; Hirosaki, N.; et al. Achieving High Quantum Efficiency Narrow-Band #-Sialon:Eu^{2+} Phosphors for High-Brightness LCD Backlights by Reducing the Eu^{3+} Luminescence Killer. *Chem. Mater.* **2018**, *30*, 494−505.
(62) Kim, Y. H.; Arunkumar, P.; Kim, B. Y.; Unithrattil, S.; Kim, E.; Moon, S.-H.; Hyun, J. Y.; Kim, K. H.; Lee, D.; Lee, J.-S.; et al. A Zero-Thermal-Quenching Phosphor. *Nat. Mater.* **2017**, *16*, 543−550.
(63) Zhang, X.; Liu, W.; Wei, G. Z.; Banerjee, D.; Hu, Z.; Li, J. Systematic Approach in Designing Rare-Earth-Free Hybrid Semiconductor Phosphors for General Lighting Applications. *J. Am. Chem. Soc.* **2014**, *136*, 14230−14236.
(64) Yamase, T. Photo- and Electrochromism of Polyoxometalates and Related Materials. *Chem. Rev.* **1998**, *98*, 307−325.
(65) Sun, C.-Y.; Wang, X.-L.; Zhang, X.; Qin, C.; Li, P.; Su, Z.-M.; Zhu, D.-X.; Shan, G.-G.; Shao, K.-Z.; Wu, H.; Li, J. Efficient and Tunable White-Light Emission of Metal−organic Frameworks by Iridium-Complex Encapsulation. *Nat. Commun.* **2013**, *4*. DOI: 10.1038/ncomms3717
(66) Asif, H. M.; Zhou, Y.; Zhang, L.; Shaheen, N.; Yang, D.; Li, J.; Long, Y.; Iqbal, A.; Li, Y. Covalent Synthesis of Two Hybrids Composed of Dawson-Type Polyoxometalate and Porphyrin with Remarkable Third-Order Optical Nonlinearities Reflecting the Effect of Polyoxometalates. *Inorg. Chem.* **2017**, *56*, 9436−9447.

DOI: 10.1021/acs.inorgchem.8b00674
Inorg. Chem. 2018, 57, 7665−7675